

Analysis of Decomposed Surface Currents in a Limited Area

Yukiharu Hisaki

Abstract—A method of the Helmholtz decomposition for mapped surface currents on grid points is developed. This method is simple, and decomposed currents are not dependent on the distance from the open boundary. This decomposition is applied to surface currents observed by high-frequency (HF) radars. The observation was conducted from April to May 1998 east of Okinawa Island, Japan. The spectral analysis of decomposed currents reveals that the M_2 tidal peak for rotational components is much smaller than that for divergent components, which suggests that the barotropic tidal components are mainly included in divergent currents. The real-vector empirical orthogonal function (EOF) analysis of decomposed currents reveals an embedded eddy, which is related with the convergence of currents.

Index Terms—Helmholtz decomposition, high-frequency (HF) radar, surface currents.

I. INTRODUCTION

AN empirical orthogonal function (EOF) analysis is often used for physical oceanography. The spatial and temporal changes of ocean data are related with various physical phenomena such as mesoscale eddies, winds, and tides. These ocean data are decomposed into orthogonal eigenfunctions, or modes using the EOF analysis. The first several of the modes generally account for a large part of the data variance. These modes are generally related to physical phenomena by investigating the relationship with other oceanic or atmospheric data. However, this method is empirical, and the isolation of physical processes is incomplete: One eigenmode may significantly be affected by more than two different physical processes. It is useful to use other decomposition methods for avoiding mixture of physical processes before EOF analysis. One of the decompositions is the time filter. The fluctuations in selected frequency bands are removed to isolate desired signals. The ocean data are decomposed into low-frequency and high-frequency (HF) fluctuations. For example, tidal frequency fluctuations are often removed to investigate low-frequency fluctuations before EOF analysis of ocean currents (e.g., [1]). The other decomposition of ocean currents is the Helmholtz decomposition. The vector \mathbf{v} can be decomposed into the sum of irrotational (divergent) \mathbf{v}_p and rotational (nondivergent) \mathbf{v}_r components as

$$\mathbf{v} = \mathbf{v}_p + \mathbf{v}_r \quad (1)$$

Manuscript received January 27, 2005; revised June 13, 2006; accepted June 29, 2006. This work was supported by the Ministry of Education, Culture, Sports, Science and Technology of Japan (16540403) under the Grant-in-Aid for Scientific Research (C-2). Associate Editor: L. Goodman.

The author is with the Physical Oceanography Laboratory, Department of Physics and Earth Sciences, University of the Ryukyus, Okinawa 903-0213, Japan (e-mail: hisaki@sci.u-ryukyu.ac.jp).

Digital Object Identifier 10.1109/JOE.2006.886082

where \mathbf{v}_p and \mathbf{v}_r satisfy

$$\nabla \times \mathbf{v}_p = 0 \quad \text{and} \quad \nabla \cdot \mathbf{v}_r = 0 \quad (2)$$

where ∇ denotes the gradient. If the vector $\mathbf{v} = \mathbf{v}(x, y)$ is the two-dimensional (2-D) current for horizontal coordinate (x, y) , \mathbf{v}_p and \mathbf{v}_r are written as

$$\mathbf{v}_p = \nabla_H \times \Psi \quad \text{and} \quad \mathbf{v}_r = \nabla_H \Phi \quad (3)$$

where ∇_H denotes the horizontal gradient, Ψ is the streamfunction, and Φ is the velocity potential.

The streamfunction Ψ and the velocity potential Φ are estimated by solving the Poisson equations as

$$\nabla_H^2 \Psi = \zeta \quad \text{and} \quad \nabla_H^2 \Phi = \xi \quad (4)$$

where $\zeta = \partial v / \partial x - \partial u / \partial y$ is the relative vorticity, and $\xi = \partial u / \partial x + \partial v / \partial y$ is the horizontal divergence. The Poisson equation (4) is numerically solved by iterative techniques. However, \mathbf{v}_p and \mathbf{v}_r are not determined uniquely only from \mathbf{v} , and other constraints such as the boundary condition of (4) are necessary to estimate \mathbf{v}_p and \mathbf{v}_r . If the analysis area of the ocean currents is a closed basin, the boundary condition at the coast completes the system [2]. However, there is no information on the boundary condition for the open boundary. Additionally, estimated \mathbf{v}_p and \mathbf{v}_r are dependent on the distance from the boundary, if the boundary condition is introduced. We introduce other constraints to estimate \mathbf{v}_p and \mathbf{v}_r uniquely.

It is necessary to observe \mathbf{v} at a high spatial resolution to estimate \mathbf{v}_p and \mathbf{v}_r . The HF radar can observe surface currents at a high spatial resolution. HF ocean radars can infer ocean surface currents [3]–[5] and waves [6]–[8] by analyzing the backscattered signals from HF radio waves, radiated over the ocean.

One of the objectives of this paper is to describe the method of the Helmholtz decomposition. In this method, the decomposed current vectors \mathbf{v}_p and \mathbf{v}_r are not dependent on the distance from the open boundary. The other objective of the paper is to demonstrate the decomposition for applying the temporal and spatial (EOF) analysis. We applied the real-vector EOF analysis [9], [10]. The real-vector EOF analysis preserves the nondivergence or irrotationality [9]. Therefore, the real-vector EOF analysis is suitable for applying to decomposed currents.

In Section II, the method of the Helmholtz decomposition and real-vector EOF analysis are described. Section III describes the observation of HF ocean radar, and presents the general features in the observation area based on previous work [4]. The result of the Helmholtz decomposition and EOF analysis is presented in Section IV. Section V presents a discussion and draws conclusions.

II. METHOD

A. Helmholtz Decomposition

The additional constraint to (1) and (2) is

$$\mathbf{v}_p \simeq r\mathbf{v}_r \simeq \frac{r}{1+r}\mathbf{v} \quad (5)$$

or

$$\alpha\mathbf{v}_p = \frac{\alpha r}{1+r}\mathbf{v} \quad (6)$$

where r is the ratio of \mathbf{v}_r to \mathbf{v}_p , $r = 1$ here, and α is the weight of for the overdetermined linear equations. Equation (5) is satisfied instead of (2) for large α .

The surface currents $\mathbf{v} = (u, v)$ are obtained at the regular grid point in the irregular domain (not rectangular domain). The x and y grid number in the domain is written as $i_x(i)$ and $i_y(i)$ ($i = 1, \dots, M$), where M is the number of grid points in the domain, and surface currents are written as $\mathbf{v}(i) = (u(i), v(i))$, $\mathbf{v}_p(i) = (u_p(i), v_p(i))$, and $\mathbf{v}_r(i) = (u_r(i), v_r(i))$ ($i = 1, \dots, M$). It was possible to store the $4M \times 4M$ matrix in the computer memory, and we solved (1), (2), and (6) directly. Equation (2) is discretized by the two-grid-point centered difference. Equations (1), (2), and (6) are written as

$$A\mathbf{s} = \mathbf{f} \quad (7)$$

where A is the $(4M + 2L) \times 4M$ matrix and $L (< M)$ is the number of grid points which are not on the boundary of the domain.

The x and y grid numbers in the domain which are not on the boundary of the domain are written as $(i_x(i), i_y(i))$ ($i = i_1, \dots, i_L$). The $4M$ -dimensional vector \mathbf{s} is

$$\mathbf{s} = (u_p(1), \dots, u_p(M), u_r(1), \dots, u_r(M), v_p(1), \dots, v_p(N), v_r(1), \dots, v_r(M)). \quad (8)$$

The matrix A denotes coefficient of (1) for matrix row number $m \leq 2M$, (6) for matrix row number $2M < m \leq 4M$, and (2) for matrix row number $m > 4M$. The $(4M + 2L)$ -dimensional vector \mathbf{f} is

$$\mathbf{f} = \left(\mathbf{V}, \frac{\alpha r}{1+r}\mathbf{V}, 0, \dots, 0 \right) \quad (9)$$

$$\mathbf{V} = (u(1), \dots, u(M), v(1), \dots, v(M)). \quad (10)$$

Most of the components of the $(4M + 2L) \times 4M$ matrix A is zero, and it is possible to express the matrix A without using a huge computer memory. The nonzero component of the matrix A is expressed in terms of $n_z(m, k)$ and $a_z(m, k)$ ($k = 1, \dots, N_z(m)$, where $n_z(m, k)$ is the k th nonzero component column number of the matrix A for row number m , $a_z(m, k)$ is the $(m, n_z(m, k))$ component of the matrix A , and $N_z(m)$ is the number of nonzero component of the matrix A for row number m . The expressions of $n_z(m, k)$, $a_z(m, k)$, and $N_z(m)$ are written in the Appendix. Because the maximum of $N_z(m)$ is 4, the memory requirement for matrix A is M times of that for matrix $a_z(m, k)$.

The overdetermined equation (7) is solved from the normal equation

$$A^T A \mathbf{s} = A^T \mathbf{f} \quad (11)$$

where subscript T denotes the transpose of the matrix. The component of the matrix $A^T A$ is calculated from $n_z(m, k)$, $a_z(m, k)$ and $N_z(m)$ using the updating equation as

$$A^T A(n_z(m, k_1), n_z(m, k_2)) \rightarrow A^T A(n_z(m, k_1), n_z(m, k_2)) + a_z(m, k_1)a_z(m, k_2) \quad (12)$$

for $m = 1, \dots, M$, $k_1 = 1, \dots, N_z(m)$, and $k_2 = 1, \dots, N_z(m)$. Similarly, the $4M$ -dimensional vector $A^T \mathbf{f}$ can be calculated from (9) and (17)–(35).

It was possible to store the matrix $A^T A$ in the computer memory in the present example. However, it may not be possible to save the matrix for large M . The matrix $A^T A$ is also sparse. In this case, only nonzero entries of the sparse matrix are stored to save computer memory as $n_z(m, k)$, $a_z(m, k)$, and $N_z(m)$. The reverse Cuthill–Mckee algorithm [11] and the Cholesky method will be applied to solve (11).

B. Real-Vector EOF Analysis

The method of real-vector EOF analysis is described in [9] and [10]. The method is briefly summarized.

The estimated currents are $\mathbf{v}(i, j) = (u, v) = (v_1, v_2)$ ($i = 1, \dots, M$, $j = 1, \dots, N$), where i is the grid number, j is the time number, and N is the total number of time series. The real-vector EOF analysis can be conducted by solving the eigenvalue problem as

$$C\mathbf{e} = \lambda\mathbf{e} \quad (13)$$

where C is the $2M \times 2M$ covariance matrix, whose (m, n) component $(m, n = 1, \dots, 2M)$ is

$$C(m, n) = \frac{1}{N} \sum_{j=1}^N \{ \tilde{v}_{[(m-1)/M]+1(\text{mod}(m-1, M)+1, j)} \times \tilde{v}_{[(n-1)/M]+1(\text{mod}(n-1, M)+1, j)} \} \quad (14)$$

where $\text{mod}(m, M)$ denotes the remainder of $m \div M$, $[\dots]$ denotes truncated integer, and a tilde ($\tilde{}$) denotes time anomaly. The K th largest eigenvalue (K th eigenmode) $\lambda = \lambda_K(\mathbf{v})$ and the $2M$ -dimensional eigenvector $\mathbf{e} = \mathbf{e}_K(\mathbf{v})$ ($K = 1, \dots, 2M$) are estimated from (13) as $|\mathbf{e}| = 1$. The time coefficient $a_K(j, \mathbf{v})$ for K th mode at time j is estimated from $\tilde{\mathbf{V}} = \tilde{\mathbf{V}}(j)$ (10) as

$$a_K(j, \mathbf{v}) = \tilde{\mathbf{V}}(j) \cdot \mathbf{e}_K(\mathbf{v}). \quad (15)$$

The eigenmode for \mathbf{v}_r and \mathbf{v}_p can be estimated by the same method as (13)–(15). The eigenvalues $\lambda_K(\mathbf{v}_r)$ and $\lambda_K(\mathbf{v}_p)$, eigenvectors $\mathbf{e}_K(\mathbf{v}_r)$ and $\mathbf{e}_K(\mathbf{v}_p)$, and time coefficients $a_K(j, \mathbf{v}_r)$ and $a_K(j, \mathbf{v}_p)$ for the K th mode are also estimated.

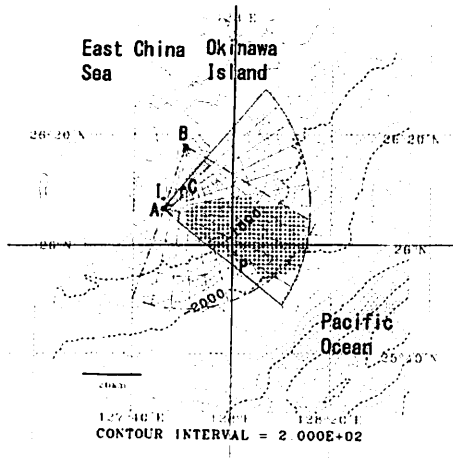


Fig. 1. Map of observation area.

III. OBSERVATION

The observation of surface currents by HF (24.5 MHz) ocean radars east of Okinawa, Japan was conducted from April to May 1998. The radar system is the phased-array system. The range resolution of the radar is 1.5 km, and the beam resolution is 7.5°. The details of the observation are described in [4]. Fig. 1 shows the observation area. The HF ocean radar measured surface currents every 2 h from shore sites at the location A (26° 7.19' N, 127° 45.78' E) and location B (26° 18.63' N, 127° 50.25' E) in Fig. 1. The period of the analysis is from 04:00:00L on April 15, 1998 to 10:00:00L on May 15, 1998, and $N = 364$. The surface currents are mapped on the 1.5-km grids in Fig. 1, and $M = 352$. Not all the grid points in the area of overlap between the two radar coverage areas are used for analysis. Over 256 time series (70% of total data available) are used at the selected grid points in Fig. 1.

The data gaps were linearly interpolated. The interpolated data was about 12% of the total data. The current meter and temperature sensor were deployed at the location P (25° 59' N, 128° 0.5' E) in Fig. 1 and at water depth 4 m from the surface. These *in situ* observed currents were compared with HF ocean radar estimated currents. The agreement between them was good, differences were less than 12 cm/s, and the correlation coefficient was greater than 0.85 for both u and v components [4]. Surface wind data at location I (26° 09' N, 127° 46' E) were observed by the Japan Meteorological Agency (JMA). The sea level data at location C (Chinen, 26° 11' N, 127° 50' E) were observed by the Geographical Survey Institute. The effect of the sea surface pressure variation on the sea level was corrected.

Most of the observation area is deep and can be characterized as open ocean rather than continental shelf. The currents are affected by mesoscale eddies. The HF ocean radars sampled a region where anticyclonic and cyclonic mesoscale eddies were adjacent to each other. The convergent zones associated with fronts of mesoscale eddies are often found during the observation period, for example, on April 16, 22, and 29 and May 2 and 5 [4].

The surface currents in regions shallower than about 1000 m had a correlation with winds. The correlation between winds and

HF radar-derived currents in the offshore region is decreased because of an increased influence of mesoscale eddies [4].

IV. RESULTS

A. General Features

The irrotational (divergent) components \mathbf{v}_p and rotational (nondivergent) components \mathbf{v}_r are obtained from HF radar observed \mathbf{v} by the method described in Section II. The value of the regularization parameter α is 10^{-3} . Equations (1) and (2) for the two-grid-point-centered difference are almost completely satisfied. The total root-mean-square (rms) values of $|\mathbf{v} - \mathbf{v}_p - \mathbf{v}_r|$, $|\nabla_H \times \mathbf{v}_p|$, and $\nabla_H \cdot \mathbf{v}_r$ are $5.15 \times 10^{-9} \text{ cm}\cdot\text{s}^{-1}$, $2.88 \times 10^{-6} \text{ cm}\cdot\text{s}^{-1}\cdot\text{km}^{-1}$, and $1.78 \times 10^{-6} \text{ cm}\cdot\text{s}^{-1}\cdot\text{km}^{-1}$, respectively. Equation (5) is approximately satisfied, which shows that the value of α is valid. We also decomposed \mathbf{v} into \mathbf{v}_p and \mathbf{v}_r by the Green's function method [12]. The estimated \mathbf{v}_p and \mathbf{v}_r do not satisfy (1) and (2) for the two-grid-point-centered difference. This is due to the inconsistency of the differentiation. The present method estimates \mathbf{v}_p and \mathbf{v}_r directly, and there are no inconsistencies in the differentiations.

Fig. 2 shows examples of surface currents \mathbf{v} and decomposed currents \mathbf{v}_p and \mathbf{v}_r at 22:00:00L on April 17, 1998 and 18:00:00L on May 5, 1998. The convergent currents can be seen along the 26° N latitude line and in the west of 128° E longitude Fig. 2(a). North of the convergent area, the currents seem to be cyclonic. A counterclockwise eddy can be seen near the coast (north of the 26° N latitude line and east of the 128° E longitude line) in Fig. 2(a). The convergent zone along the 26° N latitude line is isolated in Fig. 2(c). The clockwise currents north of the convergent area and a counterclockwise eddy are isolated in Fig. 2(e). The convergent currents can also be seen south of the 26° N latitude line in Fig. 2(b). This convergence is isolated in Fig. 2(d). The currents north of the 26° N and east of the 128° E are counterclockwise. This counterclockwise eddy is isolated in Fig. 2(f). The irrotational components \mathbf{v}_p and rotational components \mathbf{v}_r are similar west of the 128° E longitude in Fig. 2(d) and (f). Because the value of α is small ($\alpha = 10^{-3}$), $\mathbf{v}_p \neq \mathbf{v}_r$ in most of the area. In the area where both of the horizontal divergence and the relative vorticity are small, the decomposed currents are $\mathbf{v}_p \simeq \mathbf{v}_r \simeq \mathbf{v}/2$ from (6).

Fig. 3 shows time-mean surface currents \mathbf{v} , divergent currents \mathbf{v}_p , and rotational currents \mathbf{v}_r during the data analysis period. These three current maps are similar: The currents near the coast were weak and directed northeastward. Southward mean flow was observed off the coast of Okinawa Island. The fact that \mathbf{v}_p and \mathbf{v}_r are almost the same ($\mathbf{v}_p \simeq \mathbf{v}_r \simeq \mathbf{v}/2$) is that the mean currents are both nondivergent and irrotational, because $\nabla_H \cdot \mathbf{v} \simeq 0$ and $\nabla_H \times \mathbf{v} \simeq 0$.

Fig. 4 shows rotary spectra of \mathbf{v} [Fig. 4(a)], \mathbf{v}_p [Fig. 4(b)], and \mathbf{v}_r [Fig. 4(c)], estimated by the maximum entropy method (MEM) at 128.16° E and 26.11° N. Fig. 4(d) shows the ratio of the rotary spectrum of \mathbf{v}_p to the rotary spectrum of \mathbf{v}_r . The ratio of the squared kinetic energy at grid point i is also calculated as

$$K_r(i, \mathbf{v}_p) = \left\{ \frac{\sum_{j=1}^N |\mathbf{v}_p(i, j)|^2}{\sum_{j=1}^N |\mathbf{v}_r(i, j)|^2} \right\}^{-1/2} \quad (16)$$

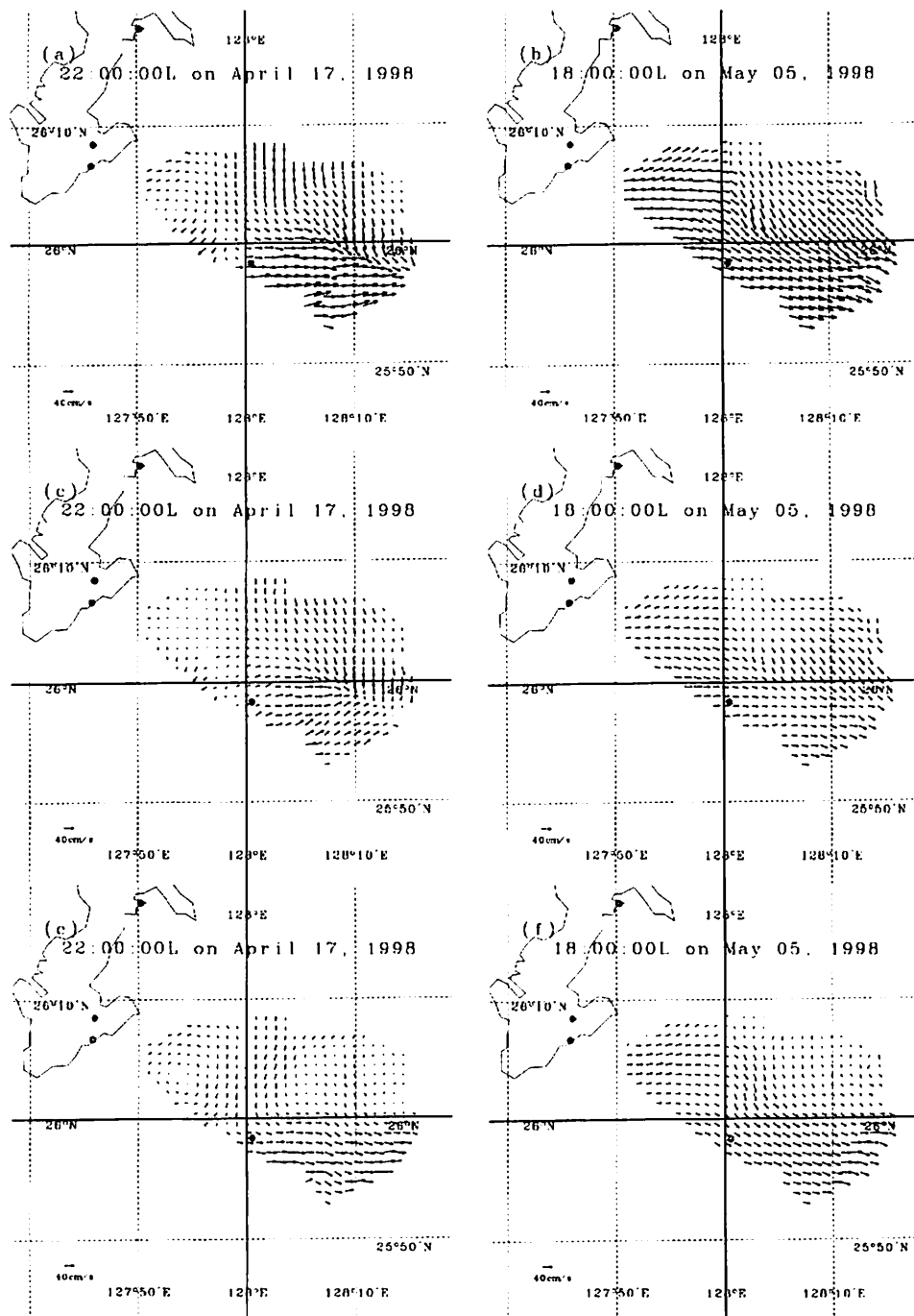


Fig. 2. Examples of current decomposition. \mathbf{v} at (a) 22:00:00L on April 17, 1998 and (b) 18:00:00L on May 5, 1998. \mathbf{v}_p at (c) 22:00:00L on April 17, 1998 and (d) 18:00:00L on May 5, 1998. \mathbf{v}_r at (e) 22:00:00L on April 17, 1998 and (f) 18:00:00L on May 5, 1998.

The values of $K_r(i, \mathbf{v}_p)$ and $K_r(i, \mathbf{v}_r)$ at the grid point are, respectively, $K_r(i, \mathbf{v}_p) = 0.537$ and $K_r(i, \mathbf{v}_r) = 0.507$, which are almost the same values. The spectral peaks corresponding to the K_1 and M_2 tides can be seen in Fig. 4(a)–(c). There are differences of tidal peaks in Fig. 4(b) and (c), especially in the M_2 tide. The M_2 tidal peak levels in Fig. 4(b) are larger than those in Fig. 4(c) and (d). The clockwise M_2 tidal peak level is close to the counterclockwise M_2 tidal peak level in Fig. 4(b), while the clockwise M_2 tidal peak level is much larger than the counterclockwise M_2 tidal peak level in Fig. 4(c). This shows that

the M_2 tidal ellipse of \mathbf{v}_p is close to being a straight line. The M_2 tidal phases are calculated from \mathbf{v}_p at the grid and sea levels at Chinen (C in Fig. 1). The difference of phases is 83° , which shows that the M_2 tidal wave of \mathbf{v}_p is the standing wave. On the other hand, the M_2 tidal wave of \mathbf{v}_r is the progressive wave. The M_2 tide includes both barotropic and baroclinic (internal) tides. The barotropic tidal component is mainly included in divergent currents \mathbf{v}_p , and M_2 tidal peak levels are large. These differences of tidal peaks for the K_1 tide are not so prominent as those for the M_2 tide. The baroclinic tide is dominant for the

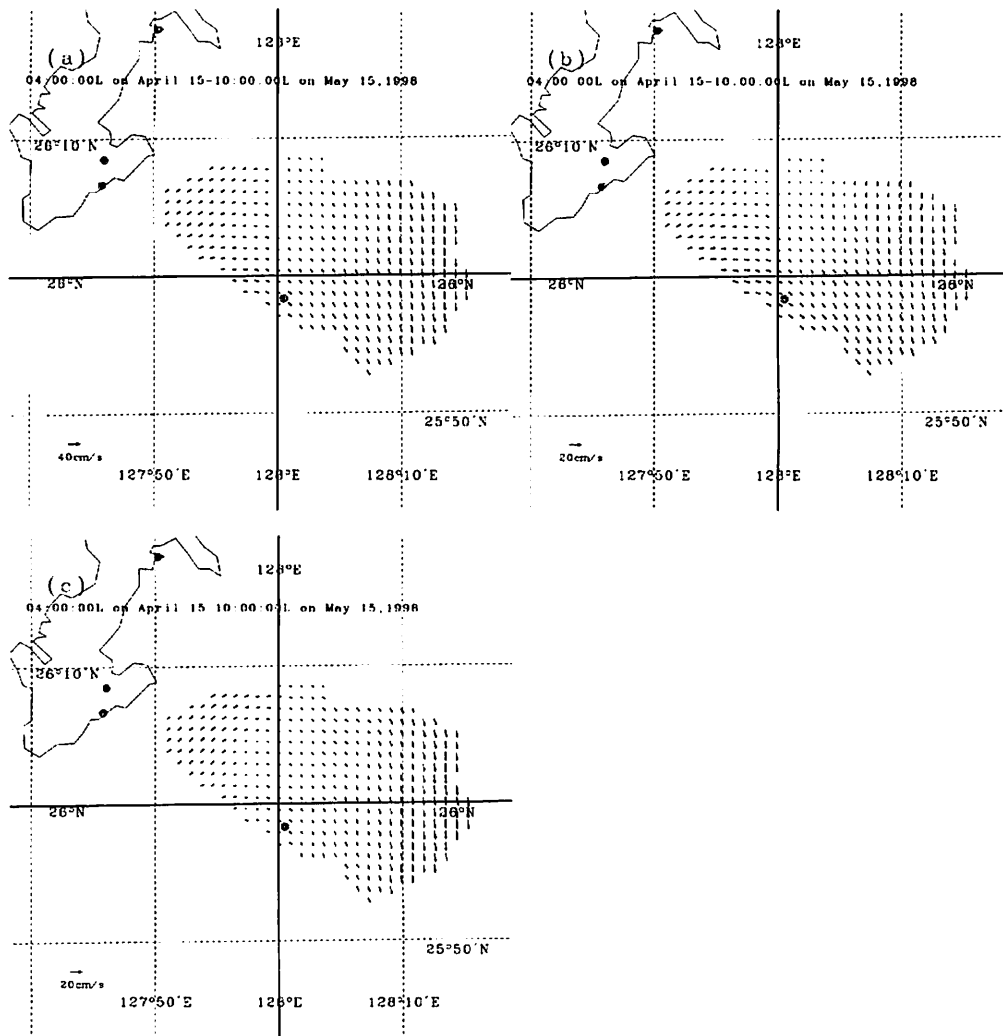


Fig. 3. Time-mean surface currents for (a) \mathbf{v} , (b) divergent currents \mathbf{v}_p , and (c) rotational currents.

K_1 tide. The amplitude and phase of the K_1 tidal components were time variables [4]. The inertial frequency at the latitude is lower than K_1 tidal frequencies, and the K_1 tidal-period fluctuations can also propagate as internal waves. These features can be seen in many grid points.

B. EOF Analysis

Fig. 5 shows cumulative variances and eigenvalues plotted against mode number K for \mathbf{v} , \mathbf{v}_p , and \mathbf{v}_r . Mode 1 of \mathbf{v} accounts for $\lambda_1(\mathbf{v})E(\mathbf{v}, 2M)^{-1} = 52.4\%$, mode 2 accounts for $\lambda_2(\mathbf{v})E(\mathbf{v}, 2M)^{-1} = 18.9\%$, and mode 3 accounts for $\lambda_3(\mathbf{v})E(\mathbf{v}, 2M)^{-1} = 9.46\%$ of the total variance, where $E(\mathbf{v}, K) = \sum_{K=1}^K \lambda_K(\mathbf{v})$. The first three EOF modes together account for $E(\mathbf{v}, 3)E(\mathbf{v}, 2M)^{-1} = 81\%$ of the variance. The eigenvalue plotted against mode number in a log-log scale (Fig. 5(b)) shows that the higher modes fall nearly on a straight line [dotted line in Fig. 5(b)]. The first three modes are above the line, and are judged to be the statistically significant [10]. Mode 1 of \mathbf{v}_p accounts for $\lambda_1(\mathbf{v}_p)E(\mathbf{v}_p, 2M)^{-1} = 49\%$, mode 2 accounts for $\lambda_2(\mathbf{v}_p)E(\mathbf{v}_p, 2M)^{-1} = 18.4\%$, and mode 3 accounts for $\lambda_3(\mathbf{v}_p)E(\mathbf{v}_p, 2M)^{-1} = 6.9\%$ of

the total variance. The first three EOF modes together account for $E(\mathbf{v}_p, 3)E(\mathbf{v}_p, 2M)^{-1} = 73\%$ of the variance, which is smaller than that of \mathbf{v} . The first three modes are also above the line of higher modes [Fig. 5(d)]. Mode 1 of \mathbf{v}_r accounts for $\lambda_1(\mathbf{v}_r)E(\mathbf{v}_r, 2M)^{-1} = 44\%$, mode 2 accounts for $\lambda_2(\mathbf{v}_r)E(\mathbf{v}_r, 2M)^{-1} = 17\%$, and mode 3 accounts for $\lambda_3(\mathbf{v}_r)E(\mathbf{v}_r, 2M)^{-1} = 15.6\%$ of the total variance. The first three EOF modes together account for $E(\mathbf{v}_p, 3)E(\mathbf{v}_p, 2M)^{-1} = 77\%$ of the variance, which is smaller than that of \mathbf{v} , and larger than that of \mathbf{v}_p . The first three modes are also above the line of higher modes [Fig. 5(f)].

Fig. 6 shows maps of eigenvectors of the first three modes for \mathbf{v} , \mathbf{v}_p , and \mathbf{v}_r ($\mathbf{e}_K(\mathbf{v})$, $\mathbf{e}_K(\mathbf{v}_p)$, and $\mathbf{e}_K(\mathbf{v}_r)$, $K = 1, 2, 3$). The eigenvectors of mode 1 are similar to each other [Fig. 6(a), (d), and (g)]. The eigenvectors are uniform and directed southwest. The scalar product of mode 1 is $\mathbf{e}_1(\mathbf{v}_p) \cdot \mathbf{e}_1(\mathbf{v}_r) = 0.96$, which shows that $\mathbf{e}_1(\mathbf{v}_p)$ is close to $\mathbf{e}_1(\mathbf{v}_r)$. The eigenvector of mode 2 for \mathbf{v}_p [Fig. 6(e)] is similar to that for \mathbf{v} [Fig. 6(b)], but not similar to that for \mathbf{v}_r [Fig. 6(h)]. The eigenvectors $\mathbf{e}_2(\mathbf{v})$ and $\mathbf{e}_2(\mathbf{v}_p)$ are almost uniform and directed southeast. In the southeast part of the HF

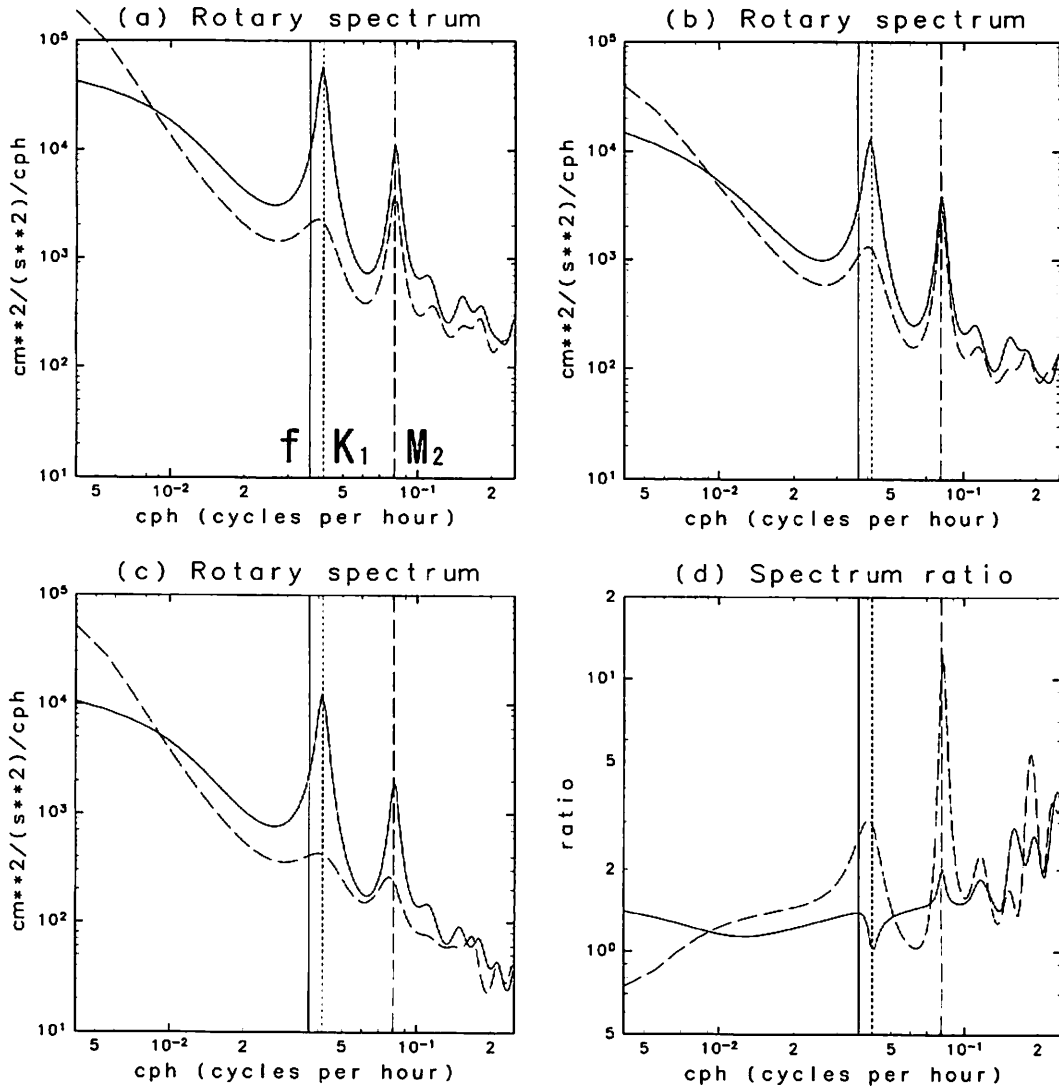


Fig. 4. Rotary spectra at 128.16° E and 26.11° N for (a) v , (b) divergent currents v_p , and (c) rotational currents v_r . (d) Ratio of rotary spectra (divergent currents/rotational currents). Solid line: clockwise. Dashed line: counterclockwise. f : inertial frequency.

ocean radar observation area, the eigenvector $e_2(v_p)$ seems to be convergent. A clockwise eddy can clearly be seen north of 26° N and east of 128° E [Fig. 6(h)]. The scalar product of the mode 2 is $e_2(v_p) \cdot e_2(v_r) = -0.15$. The eigenvector of mode 3 for v_p [Fig. 6(f)] is also similar to that for v [Fig. 6(c)], but a convergent area is prominent in Fig. 6(f). The convergent zone can be seen along the 128° E longitude line in Fig. 6(f). The vectors west of the 128° E longitude line are directed northeast, and vectors east of the 128° E longitude line are directed northwest. The magnitudes of the vectors south of 26° N are small. The vectors are convergent in this area. The magnitudes of vectors near the coast (north of 26° N and west of 128° E) are not small only in Fig. 6(f), which shows that the currents near the coast are reflected in mode 3 for v_p .

The eigenvector of mode 3 for v_r [Fig. 6(i)] is similar to that of mode 2 for v_p [Fig. 6(e)]. The vectors are directed southeast, but magnitudes of vectors near the coast are small in Fig. 6(i). The eddy-like structures can be seen, although they are not as clear as those in Fig. 6(h). The vectors west of 128° E and north

of 26° N have a counterclockwise eddy structure. The vectors in the offshore area have a clockwise eddy structure. The scalar products of eigenvectors are $e_2(v_p) \cdot e_3(v_r) = 0.93$, $e_3(v_p) \cdot e_3(v_r) = -0.002$, and $e_3(v_p) \cdot e_2(v_r) = 0.43$, respectively.

Fig. 7 shows time series of coefficients $a_K(j, v)$, $a_K(j, v_p)$, and $a_K(j, v_r)$ for K th mode at time j ($K = 1, 2, 3, j = 1, \dots, N$). The time series of mode 1 for v_p [$a_1(j, v_p)$: Fig. 7(d)] is similar to that for v [Fig. 7(a)] and that for v_r [Fig. 7(g)]. The correlation coefficient between $a_1(j, v_p)$ and $a_1(j, v_r)$ is $R_c(a_1(j, v_p), a_1(j, v_r)) = 0.99$. The first mode is nondivergent and irrotational.

The time series of mode 2 for v_p [$a_2(j, v_p)$: Fig. 7(e)] is similar to that for v [Fig. 7(b)]. However, the time series of $a_2(j, v_p)$ is not similar to $a_2(j, v_r)$ [Fig. 7(h)] but similar to $a_3(j, v_r)$ [Fig. 7(i)]. Their correlation coefficients are $R_c(a_2(j, v_p), a_2(j, v_r)) = -0.15$ and $R_c(a_2(j, v_p), a_3(j, v_r)) = 0.98$. The eigenvectors $e_2(v_p)$ and $e_3(v_r)$ are also similar to each other. The time series of $a_3(j, v_p)$ [Fig. 7(f)] is similar to $a_3(j, v)$ and

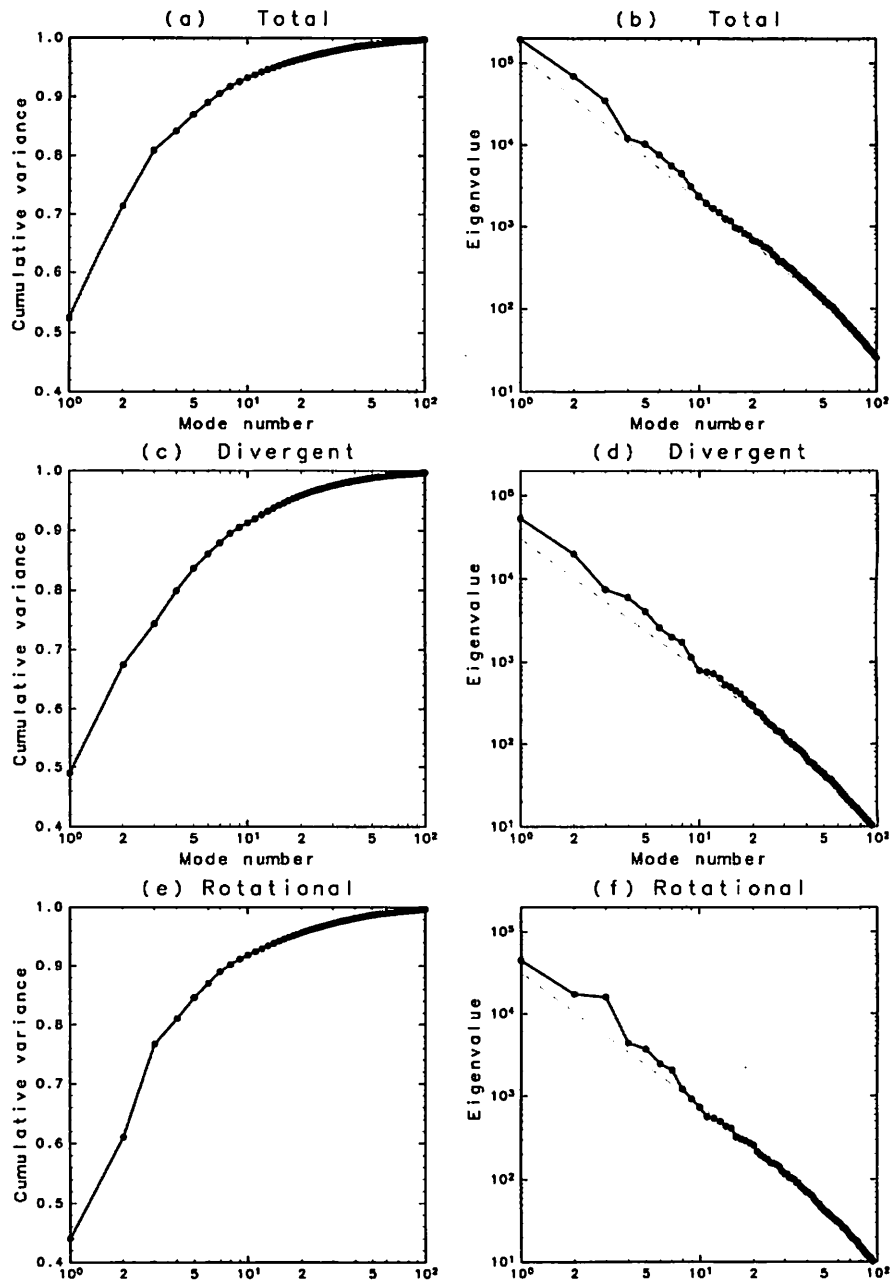


Fig. 5. (a) Cumulative variance against mode number K for \mathbf{v} . (b) Eigenvalue against mode number K for \mathbf{v} . (c) Cumulative variance against mode number K for \mathbf{v}_p . (d) Eigenvalue against mode number K for \mathbf{v}_p . (e) Cumulative variance against mode number K for \mathbf{v}_r . (f) Eigenvalue against mode number K for \mathbf{v}_r . Dotted lines in (b), (d), and (f) are used to judge the significance of EOF modes.

$a_2(j, \mathbf{v}_r)$. It is not similar to $a_3(j, \mathbf{v}_r)$. Their correlation coefficients are $R_c(a_3(j, \mathbf{v}_p), a_2(j, \mathbf{v}_r)) = 0.71$ and $R_c(a_3(j, \mathbf{v}_p), a_3(j, \mathbf{v}_r)) = 0.06$. The coefficients of mode 2 for \mathbf{v}_p are correlated with those of mode 2 for \mathbf{v}_r . The eddy in Fig. 6(h) is related to the convergent or divergent area in Fig. 6(f).

C. Comparison With Other Data

The correlations between the time-dependent coefficients ($a_K(j, \mathbf{v}_p)$ or $a_K(j, \mathbf{v}_r)$) at 2-h interval and other hourly *in situ* observations are estimated. The correlation between the

detrended 26-h running mean time-dependent coefficients and detrended 25-h running mean sea levels at 2 h interval is estimated for \mathbf{v}_p and \mathbf{v}_r and for EOF mode numbers $K = 1, 2, 3$. Because 26-h running mean time-dependent coefficients are not statistically independent of each other, and 25-h running mean sea levels are not statistically independent of each other, the effective degrees of freedom N_e [13] are estimated to assess the significance of the correlation.

The correlation coefficient is the largest for $a_1(j, \mathbf{v}_p)$ (first mode), and the value is 0.53. This correlation coefficient is significant at the 90% confidence level for the effective degrees of

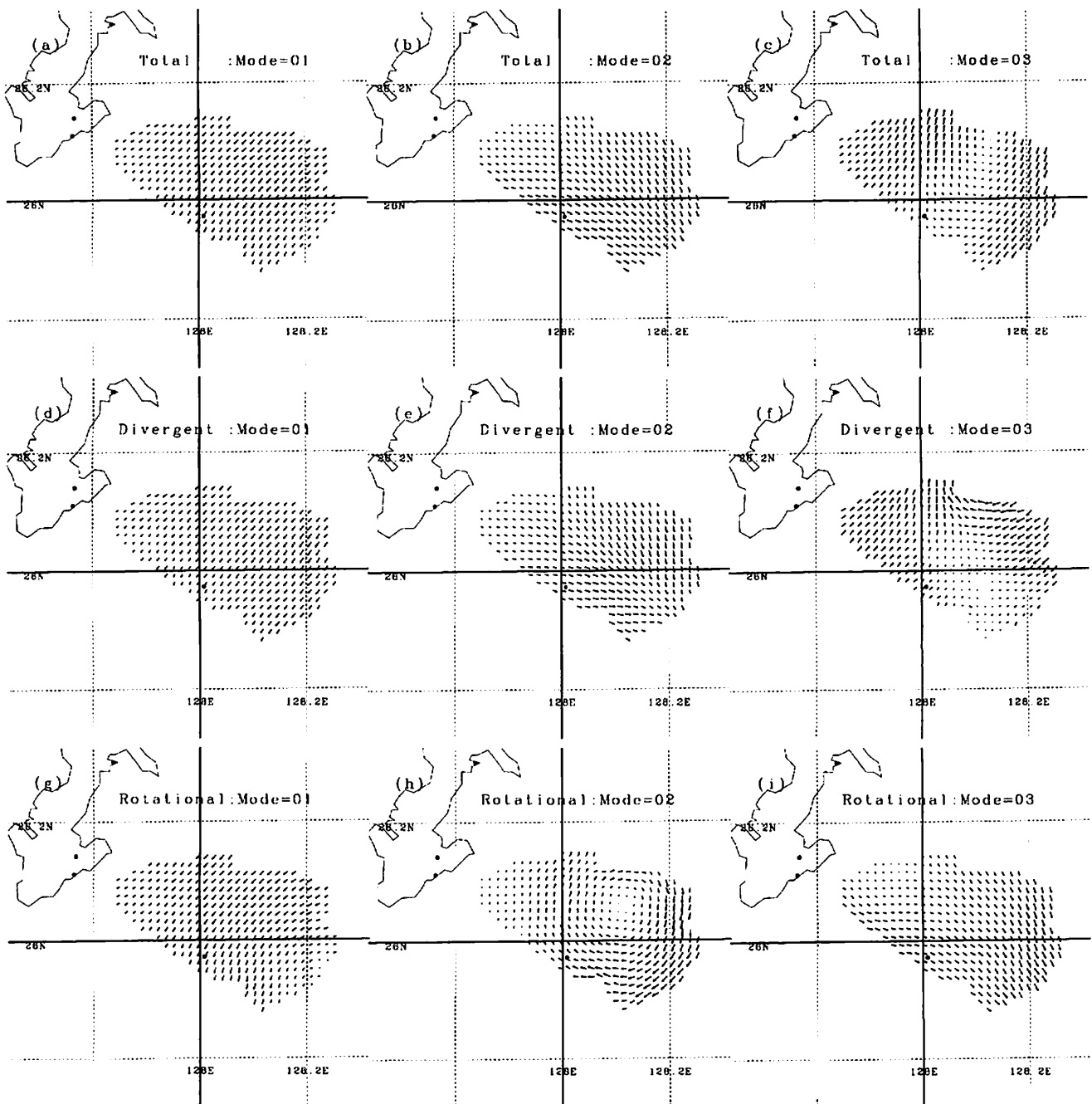


Fig. 6. (a) Eigenvectors of mode 1 for \mathbf{v} , (b) same as (a) but of mode 2, (c) same as (b) but of mode 3, (d) same as (a) but for \mathbf{v}_p , (e) same as (b) but for \mathbf{v}_p , (f) same as (c) but for \mathbf{v}_p , (g) same as (a) but for \mathbf{v}_r , (h) same as (b) but for \mathbf{v}_r , and (i) same as (c) but for \mathbf{v}_r .

freedom $N_e = 14$. The correlation coefficient for $a_1(j, \mathbf{v}_r)$ is 0.51, which is also significant at the 90% confidence level.

Fig. 8(a) shows time series of 26-h running mean time-dependent coefficients ($a_1(j, \mathbf{v}_p)$) and Fig. 8(b) shows 25-h running mean sea levels. Because tides are strong, tidal signals cannot be removed completely by the box filter in Fig. 8(b). Both values become larger on April 20, April 26, and May 1, 1998. The currents in most of the HF radar observation area are affected by the mesoscale eddy. Mode 1 relates to the change of mesoscale eddies. If the southwestward currents are dominant in the HF

radar observation area, the sea levels at Chinen (C in Fig. 1) are high. This relationship is consistent with Fig. 6(d), in which the eigenvectors are directed southwestward. The positive sea level fluctuations are associated with mode 1 southwestward flow on the shelf and are due to the presence of a cyclonic eddy offshore.

The correlations between the detrended 26-h running mean time-dependent coefficients and detrended 25-h running mean water temperatures at location P (Fig. 1) are also estimated. The maximum correlation is -0.60 for $a_1(j, \mathbf{v}_p)$, which is significant at the 90% confidence level for the effective degrees of

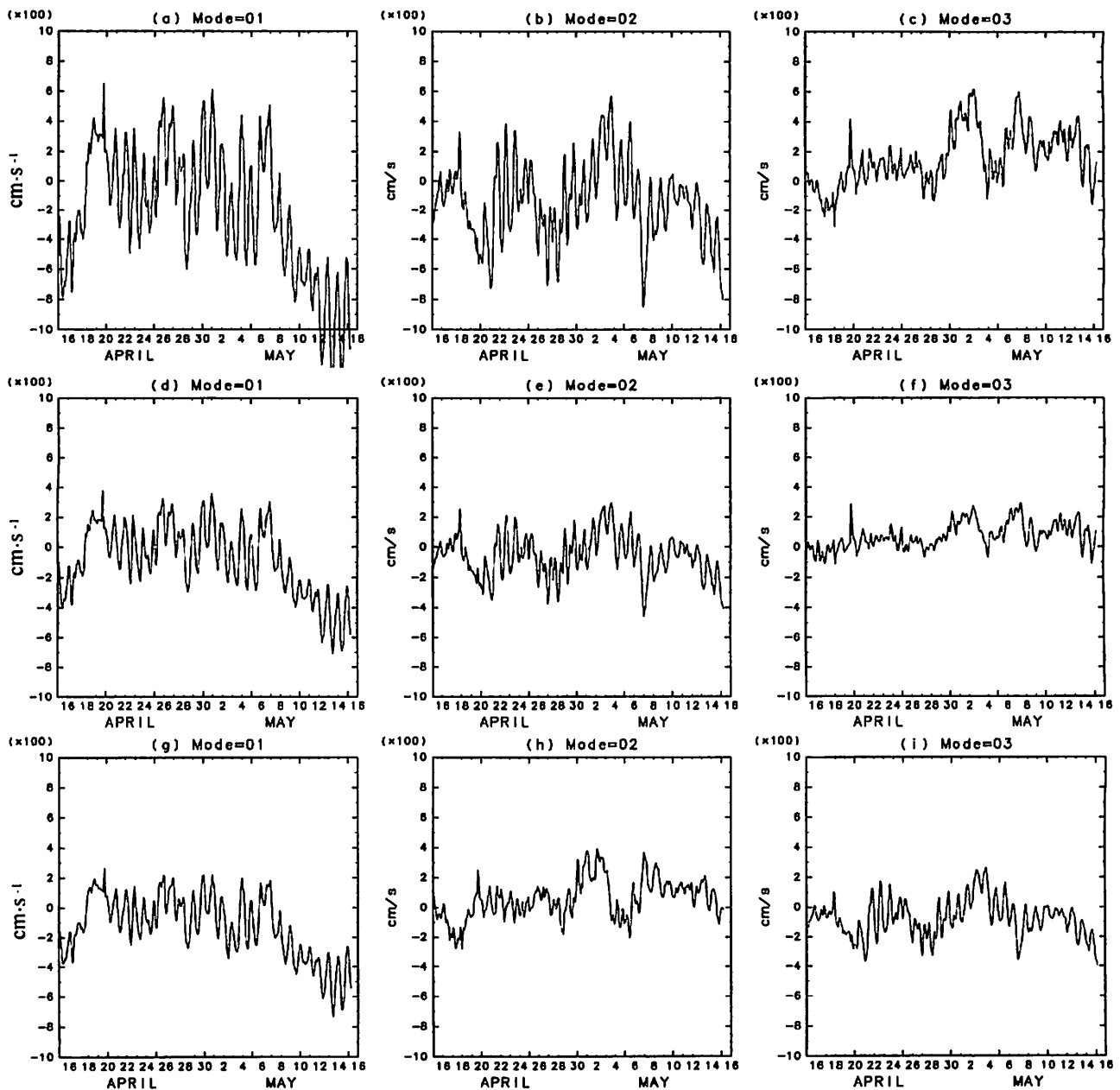


Fig. 7. (a) Time-dependent coefficients of mode 1 for \mathbf{v} . (b) Time-dependent coefficients of mode 2 for \mathbf{v} . (c) Time-dependent coefficients of mode 3 for \mathbf{v} . (d) Time-dependent coefficients of mode 1 for \mathbf{v}_p . (e) Time-dependent coefficients of mode 2 for \mathbf{v}_p . (f) Time-dependent coefficients of mode 3 for \mathbf{v}_p . (g) Time-dependent coefficients of mode 1 for \mathbf{v}_r . (h) Time-dependent coefficients of mode 2 for \mathbf{v}_r . (i) Time-dependent coefficients of mode 3 for \mathbf{v}_r .

freedom $N_e = 10$. The correlation for $a_1(j, \mathbf{v}_r)$ is -0.59 , which is also significant at the 90% confidence level. Fig. 8(c) shows 25-h running mean water temperatures at location P. The temperature becomes lower on April 20, April 26, and May 1, 1998, when the time-dependent coefficients $a_1(j, \mathbf{v}_p)$ are larger. The current vectors are southwestward in the lower water temperature case, which is consistent with Fig. 6(d).

V. DISCUSSION AND CONCLUSION

A method of Helmholtz decomposition of surface current vectors sampled on grid points in a limited domain is developed. This

method is simple, and decomposed vectors are not affected by the open boundary condition. The computer memory problem can be avoided by storing only nonzero entries of the sparse matrix. The method estimates \mathbf{v}_p and \mathbf{v}_r directly. Estimated vectors \mathbf{v}_p and \mathbf{v}_r satisfy (1) and (2). The rotary spectra of decomposed current vectors are calculated. The M_2 tidal peak for \mathbf{v}_r is much smaller than that for \mathbf{v}_p . The M_2 barotropic tidal wave in the area propagates northwestward [14] and back. The M_2 tidal wave for \mathbf{v}_p behaves as a standing wave. These results show that the M_2 tide is primarily barotropic and divergent. It may be possible to isolate the barotropic tide from tidal currents by utilizing the method.

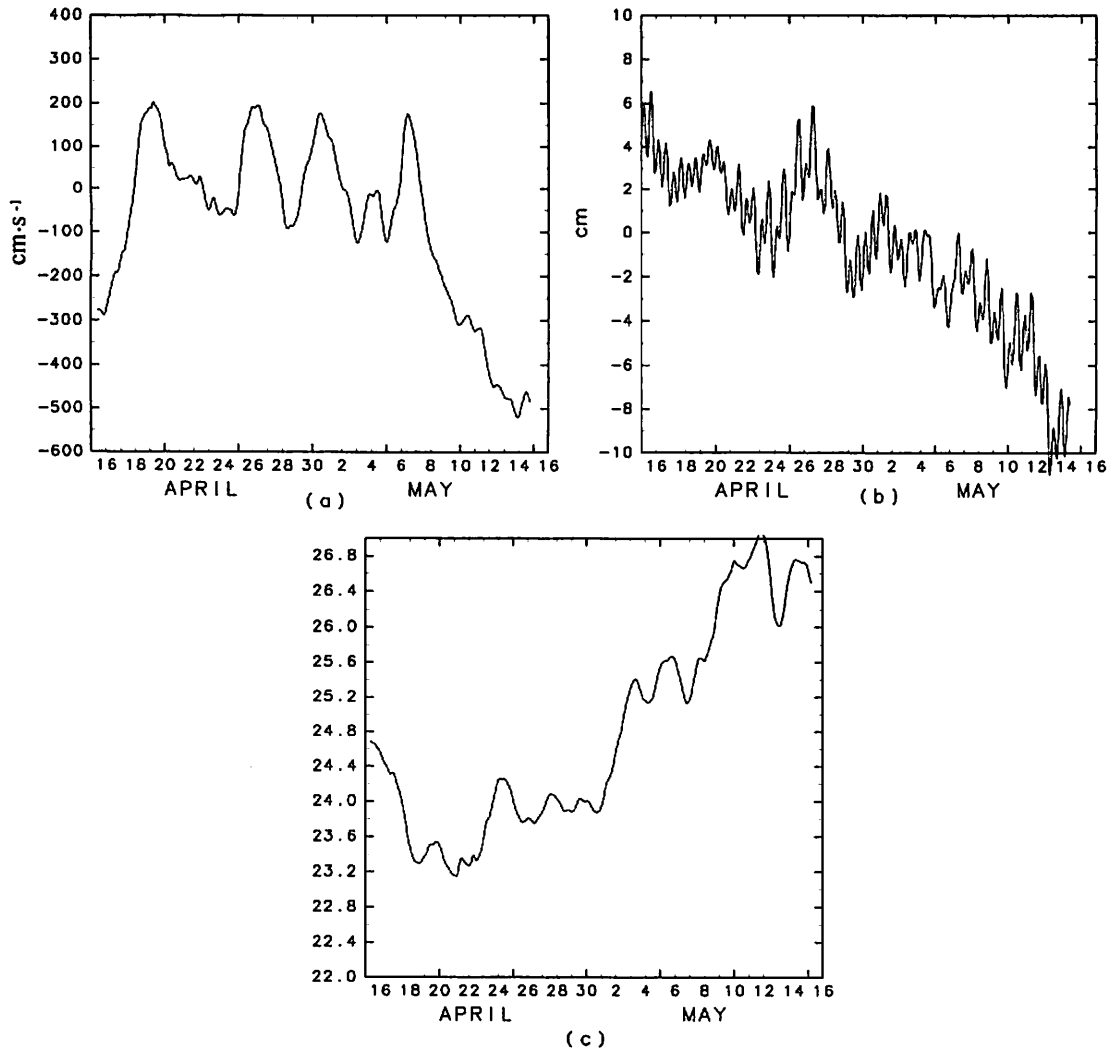


Fig. 8. (a) 26-h running mean time-dependent coefficients of mode 1 for v_p ($u_1(j, v_p)$). (b) 25-h running mean sea levels at location C in Fig. 1. (c) 25-h running mean water temperatures ($^{\circ}\text{C}$) at location P.

The real-vector EOF is applied to decomposed currents. The variances of each EOF mode for v_p are similar to those for v_r . The eigenvectors and time-dependent coefficients of EOF mode 1 for v_p are similar to those for v_r . The time-dependent coefficients for mode 1 are correlated with sea level data and sea water temperatures, which shows mode 1 is related to a mesoscale eddy. The EOF mode 2 for v_p and the EOF mode 3 for v_r are similar and show cross-shore components of currents. Mode 2 for v_r shows the embedded eddy. Although the physical mechanism of the eddy is unclear, the eddy is related to mode 3 of divergent currents. If the eddy is anticyclonic, its center is convergent. It is possible to investigate the relationship between the eddy and the divergence or convergence by using the Helmholtz decomposition.

The observed surface currents are the sum of geostrophic currents, wind driven Ekman currents, barotropic and baroclinic tidal currents, higher frequency currents, and so on. By using time filters and Helmholtz decomposition, a method to decompose observed surface currents could be developed.

APPENDIX

FORM OF $n_z(m, k)$, $a_z(m, k)$, AND $N_z(m)$

The form of $n_z(m, k)$, $a_z(m, k)$, and $N_z(m)$ are expressed as follows:

$$n_z(m, 1) = m \quad n_z(m, 2) = m + M \tag{17}$$

$$a_z(m, 1) = a_z(m, 2) = 1, \quad \text{for } m \leq M \tag{18}$$

$$n_z(m, 1) = m + M \quad n_z(m, 2) = m + 2M \tag{19}$$

$$a_z(m, 1) = a_z(m, 2) = 1, \quad \text{for } M < m \leq 2M \tag{20}$$

$$n_z(m, 1) = m - 2M \quad a_z(m, 1) = \alpha, \tag{21}$$

for $2M < m \leq 3M$

$$n_z(m, 1) = m - M \quad a_z(m, 1) = \alpha, \tag{22}$$

for $3M < m \leq 4M$

$$n_z(m, 1) = i_{m-4M}^{(0,-)} \quad n_z(m, 2) = i_{m-4M}^{(0,+)} \tag{23}$$

$$n_z(m, 3) = i_{m-4M}^{(-,0)} + 2M \tag{24}$$

$$n_z(m, 4) = i_{m-4M}^{(+,0)} + 2M \tag{25}$$

$$a_z(m, 1) = a_z(m, 4) = 1 \quad a_z(m, 2) = a_z(m, 3) = -1, \\ \text{for } 4M < m \leq 4M + L \quad (26)$$

$$n_z(m, 1) = i_{m-4M-L}^{(-,0)} + M \quad (27)$$

$$n_z(m, 2) = i_{m-4M-L}^{(+,0)} + M \quad (28)$$

$$n_z(m, 3) = i_{m-4M-L}^{(0,+)} + 3M \quad (29)$$

$$n_z(m, 4) = i_{m-4M-L}^{(0,-)} + 3M \quad (30)$$

$$a_z(m, 1) = a_z(m, 4) = -1 \quad a_z(m, 2) = a_z(m, 3) = 1, \\ \text{for } 4M + L < m \leq 4M + 2L. \quad (31)$$

The grid numbers in the domain $i_l^{(-,0)}$, $i_l^{(+,0)}$, $i_l^{(0,-)}$, and $i_l^{(0,+)}$ ($l = 1, \dots, L$) are decided as

$$(i_x(i_l^{(-,0)}), i_y(i_l^{(-,0)})) = (i_x(i_l) - 1, i_y(i_l)) \quad (32)$$

$$(i_x(i_l^{(+,0)}), i_y(i_l^{(+,0)})) = (i_x(i_l) + 1, i_y(i_l)) \quad (33)$$

$$(i_x(i_l^{(0,-)}), i_y(i_l^{(0,-)})) = (i_x(i_l), i_y(i_l) - 1) \quad (34)$$

$$(i_x(i_l^{(0,+)}), i_y(i_l^{(0,+)})) = (i_x(i_l), i_y(i_l) + 1) \quad (35)$$

where i_l is the grid number in the domain which is not on the boundary. The number of nonzero component of matrix A for row number m is $N_z(m) = 2$ for $m \leq 2M$, $N_z(m) = 1$ for $2M < m \leq 4M$, and $N_z(m) = 4$ for $4M < m \leq 4M + 2L$.

ACKNOWLEDGMENT

The author would like to thank the staff of the Okinawa Radio Observatory, the Communications Research Laboratory (Okinawa Subtropical Environment Remote-Sensing Center, the National Institute of Information and Communications Technology), the Geographical Survey Institute, and Japan Meteorological Agency for providing the Doppler spectra, tidal and meteorological data, respectively. He would also like to thank the reviewer for valuable comments. The GFD-DENNOU Library (<http://dennou.gaia.h.kyoto-u.ac.jp/arch/dcl/>) was used for drawing the figures.

REFERENCES

- [1] M. N. Tsimplis, A. F. Velegrakis, A. Theocharis, and M. B. Collins, "Low-frequency current variability at the Straits of Crete, eastern Mediterranean," *J. Geophys. Res.*, vol. 102, pp. 25 005–25 020, 1997.
- [2] I. G. Watterson, "Decomposition of global ocean currents using a simple iterative method," *J. Atmos. Ocean. Technol.*, vol. 18, pp. 691–703, 2001.
- [3] H. Takeoka, Y. Tanaka, Y. Ohno, Y. Hisaki, A. Nadai, and H. Kuroiwa, "Observation of the Kyucho in the Bungo channel by HF radar," *J. Oceanogr.*, vol. 51, pp. 699–711, 1995.
- [4] Y. Hisaki, W. Fujiie, T. Tokeshi, K. Sato, and S. Fujii, "Surface current variability east of Okinawa Island obtained from remotely sensed and in-situ observational data," *J. Geophys. Res.*, vol. 106, pp. 31 057–31 073, 2001.
- [5] Y. Hisaki and T. Naruke, "Horizontal variability of near-inertial oscillations associated with the passage of a typhoon," *J. Geophys. Res.*, vol. 108, 2003, doi: 10.1029/2002JC001683, 3382.
- [6] Y. Hisaki, "Nonlinear inversion of the integral equation to estimate ocean wave spectra from HF radar," *Radio Sci.*, vol. 31, pp. 25–39, 1996.
- [7] —, "Short-wave directional properties in the vicinity of atmospheric and oceanic fronts," *J. Geophys. Res.*, vol. 107, 2002, doi: 10.1029/2001JC000912, 3188.
- [8] —, "Short-wave directional distribution for first-order Bragg echoes of the HF ocean radars," *J. Atmos. Ocean. Technol.*, vol. 21, pp. 105–121, 2004.
- [9] J. Kaihatu, M. R. A. Handler, G. O. Marmorino, and L. K. Shay, "Empirical orthogonal eigenfunction analysis of ocean surface currents using complex and real-valued methods," *J. Atmos. Ocean. Technol.*, vol. 15, pp. 927–941, 1998.
- [10] G. O. Marmorino, L. K. Shay, B. K. Haus, R. A. Handler, H. C. Graber, and M. P. Horne, "An EOF analysis of HF doppler radar current measurements of the Chesapeake Bay buoyant outflow," *Cont. Shelf Res.*, vol. 19, pp. 271–288, 1999.
- [11] J. L. Sherman, "Comparative analysis of the Cuthill-McKee and the reverse Cuthill-McKee ordering algorithms for sparse matrices," *SIAM J. Numerical Anal.*, vol. 13, pp. 198–213, 1975.
- [12] C. H. Bishop, "Domain-independent attribution. Part I: Reconstructing the wind from estimates of vorticity and divergence using free space Green's functions," *J. Atmos. Sci.*, vol. 53, pp. 241–252, 1996.
- [13] W. J. Emery and R. E. Thompson, "Statistical methods and error handling," in *Data Analysis Methods in Physical Oceanography*. Oxford, U.K.: Pergamon, 1998, pp. 193–304.
- [14] S. Ogura, "The tides in the seas adjacent to Japan," *Bull. Hydrograph. Dept.*, vol. 7, pp. 1–189, 1933.



Yukiharu Hisaki received the B.S. degree in earth science in 1988 and the M.S. degree in physical oceanography in 1990, both from the University of Tokyo, Tokyo, Japan, and the Ph.D. degree in physical oceanography in 1996 from the Tohoku University, Sendai-shi, Japan.

He is currently a Professor in the Department of the Physics and Earth Sciences, University of the Ryukyus, Okinawa, Japan. He has authored and coauthored over 40 journals, books, and conference papers. His research interests are the development of the method to estimate ocean wave spectra from HF radar, observation of surface currents using HF radar, and radio wave scattering from the sea surface.

Dr. Hisaki is a member of the Oceanographic Society of Japan, the Meteorological Society of Japan, the American Meteorological Society, and the American Geophysical Union.